Porosity and thermal collapse measurements of H₂O, CH₃OH, CO₂, and H₂O:CO₂ ices

K. Isokoski, J.-B. Bossa,* T. Triemstra and H. Linnartz*

The majority of astronomical and laboratory based studies of interstellar ices have been focusing on ice constituents. Ice structure is a much less studied topic. Particularly the amount of porosity is an ongoing point of discussion. A porous ice offers more surface area than a compact ice, for reactions that are fully surface driven. In this paper we discuss the amount of compaction for four different ices – H_2O, CH_3OH, CO_2 and mixed $H_2O : CO_2 = 2 : 1$ – upon heating over an astronomically relevant temperature regime. Laser interference and Fourier transform infrared spectroscopy are used to confirm that for amorphous solid water the full signal loss of dangling OH bonds is not a proof for full compaction. These data are compared with the first compaction results for pure CH_3OH, pure CO_2 and mixed $H_2O : CO_2 = 2 : 1$ ice. Here we find that thermal segregation benefits from a higher degree of porosity.

1 Introduction

Amorphous solid water (ASW) is the main component of interstellar and cometary ices.[1,2] Other molecular components have been identified in the solid state as well – specifically CO_2, CO, NH_3, CH_4, and CH_3OH[3] – that are embedded in or frozen on top of the water matrix, depending on the cosmo-chemical history of the ice. Chemical compositions of interstellar ices are determined by gas-grain accretion and solid state reactions. The low temperature structure of pure water ice has been extensively studied in the laboratory (see Baragiola *et al.*[4] and Loerting *et al.*[5] for reviews). Other processes further influence water ice morphology such as thermal processing, VUV photolysis and atom or electron impact. Whereas many observational studies in the past have been focusing on which constituents can be detected in their frozen state, much less is known about ice mixture structure and its effect on chemical reactivity. Agreement exists about the fact that ices in space are typically amorphous, but the amount of porosity is still under debate. This is unfortunate, as solid state astrochemical processes rely largely on surface accessibility. Porous ices provide large effective surface areas for adsorption of atoms and molecules, catalysis of chemical reactions, and further retention of the involved species. In the case of pure H_2O ice, the internal surface area can reach hundreds of $m^2 g^{-1}$.[6,7] Large quantities of molecules can be stored inside pores and later thermally released.[8–10] Remote observations, however, hint for compact (non-porous) ice structures, largely inferred from the non-detection of dangling O–H

features (2.7 μm), which are characteristic of surface water molecules.[11,12] This observation provides information on the origin of solid water in space. H_2O ice formation through surface reactions (*e.g.*, $O_2 + H$) results in a compact structure,[13] whereas gas phase H_2O condensation using omni-directional background deposition onto cryogenically cooled surfaces leads to highly porous structures.[14,15] Laboratory studies show that in the first case no dangling O–H bonds are seen, whereas in the latter case such bands are clearly visible. Formation of porous ices in the interstellar medium through vapour deposition is expected to occur in dark clouds[16,17] and in shock regions or outflows, where frozen molecules are sputtered in the gas phase and then redistributed on the remaining cold surfaces. Vapour deposition processes likely occur in proto-planetary disks where material is transported back and forth across the snow line.[18] The astronomical non-detection of dangling O–H bonds in such environments is explained by energetic processing in the interstellar medium (ISM) that is expected to cause ice compaction (*i.e.*, porosity decrease) as experimentally demonstrated by exposing interstellar ice analogues to cosmic rays, ultraviolet photons and thermal annealing.[19–23] Many of the ice observations covering the 2.7 μm region are targeting embedded sources with processed ices, where compaction indeed may have already occurred.[1,2] Given the diversity of astronomical ice environments, the absence of porosity in interstellar ices is therefore not conclusive.[24,25] The porous to compact transition will have non-negligible consequences on the overall solid state astrochemical network: a structural collapse at low temperatures can enhance the limited recombination of reactive species normally trapped in the ice matrix.

The present study focuses on a quantitative determination of ice porosity and thermal compaction and the processes at work.

Raymond and Beverly Sackler Laboratory for Astrophysics, Leiden Observatory, Leiden University, P.O. Box 9513, NL 2300 RA Leiden, The Netherlands. E-mail: bossa@strw.leidenuniv.nl, linnartz@strw.leidenuniv.nl

We have recently employed laser optical interference as a technique to monitor the thermally induced thickness decrease of porous ASW.[23] Following recent instrumental improvements we are now more sensitive to changes in ice thickness, in particular during thermal annealing. Here, we present in more detail the optical constants and the link between initial porosity and total thickness decrease of porous H_2O ice. We furthermore present the first quantitative porosity/compaction results for pure CH_3OH and CO_2 ices. The measured abundance of CH_3OH in the ISM ranges from a few up to 25% with respect to water ice.[26,27] Recent laboratory experiments have focused on the irradiation of CH_3OH dominated ices by means of VUV photons,[28] showing that a number of complex molecules as large as nine atoms can be formed, and astronomical observations confirm that CH_3OH is an archetypical interstellar molecule reputed to promote molecular complexity following VUV irradiation.[29] Methanol is assumed to form upon hydrogenation of solid CO[30,31] and spectroscopy has shown that CH_3OH preferably resides in water poor ice[32] in contrast to CO_2. Spectra are fully consistent with CH_3OH and CO intimately mixed in the ice, and consequently the present study is a first step towards more complex ices comprising two different components. As CO_2 is much more abundant in the solid state than in the gas phase, it is generally assumed that CO_2 forms on icy dust grains. Different reaction schemes have been proposed (see Ioppolo et al.[33] and Isokoski et al.[34] for recent overviews). Typically, CO_2 in space is embedded in water ice, with relative abundances varying from 15 to 40% in dark clouds. For this reason, not only pure H_2O and CO_2 ice but also mixed $H_2O:CO_2$ ice is studied here.

This manuscript is organised as follows. Section 2 describes details of experiment and data analysis. Section 3 presents the results obtained during both deposition and thermal annealing of H_2O, CH_3OH, CO_2 and $H_2O:CO_2 = 2:1$ ice samples, and is followed by a discussion. The final section summarizes the results and discusses the astronomical relevance.

2 Experimental approach

2.1 Sample preparation

The experimental setup originally described in Gerakines et al.[35] has been adapted to the configuration depicted in Fig. 1. A stainless steel chamber is evacuated using a turbo-molecular pump (Pfeiffer TPH 170) and a mechanical pump (Edwards E2M8) equipped with an oil mist filter to a base pressure of $(2.6 \pm 0.1) \times 10^{-7}$ Torr at room temperature. Ice samples are grown on a silicon substrate located in the centre of the vacuum chamber. The substrate is mounted on a closed-cycle helium cryostat that, in conjunction with resistive heating, allows for temperature control from 15 to 300 K with a relative precision of 0.1 K (Lakeshore 330). Samples are prepared in a 2 L glass bulb with a total pressure of 20 ± 1 mbar. The large volume ensures a constant deposition rate. We use milli-Q grade H_2O, CH_3OH (Aldrich, 99.8% purity) that are further purified by three freeze–pump–thaw cycles and CO_2 (Praxair, 99.998% purity).
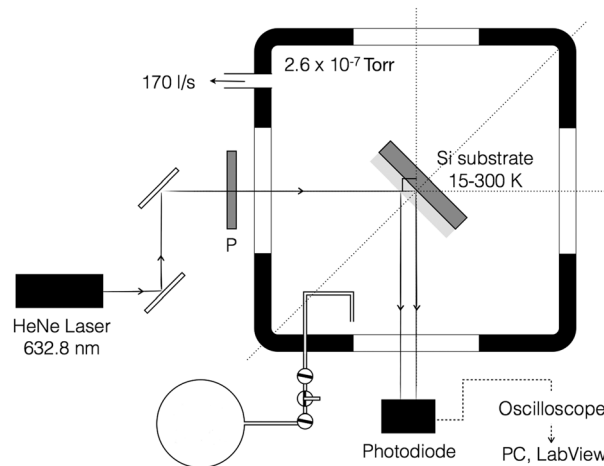

Fig. 1 Schematic drawing of the experimental setup used to measure thin-film interference in pure H_2O and CH_3OH ices. P = linear polarizer.

Samples are introduced into the vacuum chamber through a needle valve. The ices are grown by background deposition, i.e., the gas inlet is directed away from the substrate surface. This method allows the molecules to impinge onto the substrate surface with random trajectories, thus producing a porous ice structure.[14,15,36,37] The pressure in the chamber during deposition is set to $(1.0 \pm 0.1) \times 10^{-5}$ Torr. The deposited ice samples can be thermally annealed at a constant rate of 2 K min^{-1} until complete desorption.

2.2 Optical interference

The thickness and refractive index of different ice samples are derived during both deposition and thermal annealing by using optical laser interference. The interference of coherent light reflecting off the two interfaces of a thin film depends on the optical properties of the involved media, as well as the thickness of the film. We employ an intensity stabilized HeNe laser (λ = 632.8 nm) (Thorlabs HRS015) aligned through a linear polarizer which is placed in the beam path admitting only s-polarized light (perpendicular with respect to the plane of incidence). The laser beam strikes the substrate surface at an incident angle θ_0 = 45°. For the purpose of the interference experiment, a porous ice film with nm-scale surface features is considered as an effectively flat surface to the laser beam (spot size 2 mm). The reflected light is collected with a photodiode (Thorlabs PDA36A) and digitized using an oscilloscope (Textronix TDS 2022B). The photodiode signal together with the time and the temperature is recorded using the LabVIEW 8.6 software package (National Instruments).

In a three-phase layered structure (vacuum, ice, and the substrate), the effective reflection coefficient R can be written as[15,38]

$$R = \frac{r_{01} + r_{12}e^{-i2\beta}}{1 + r_{01}r_{12}e^{-i2\beta}}, \tag{1}$$

with

$$\beta = \frac{2\pi d}{\lambda} \times n_1 \cos\theta_1, \tag{2}$$

where r_{01} and r_{12} are the Fresnel reflection coefficients of the vacuum/ice and ice/substrate interfaces, d is the thickness of the ice, λ is the wavelength of the laser and n_1 is the refractive index of the ice. The incident angles θ_0 and θ_1 are related through $n_0 \sin \theta_0 = n_1 \sin \theta_1$ (Snell's law). For s-polarized light the Fresnel reflection coefficients can be written as

$$r_{01s} = \frac{n_0 \cos \theta_0 - n_1 \cos \theta_1}{n_0 \cos \theta_0 + n_1 \cos \theta_1}, \tag{3}$$

and

$$r_{12s} = \frac{n_1 \cos \theta_1 - n_2 \cos \theta_2}{n_1 \cos \theta_1 + n_2 \cos \theta_2}, \tag{4}$$

where n_0 and n_2 are the complex refractive indices of the vacuum and the silicon substrate, respectively. We use constant refractive indices $n_0 = 1$ (vacuum) and $n_2 = 3.85 - 0.07i$ (silicon substrate).[39] We relate the measurable photodiode signal S (in volts) to the reflected light intensity $|R|^2$ through an empirical scaling factor α which is intrinsic to the photodiode and that translates light intensity in volts

$$S(n_1, \alpha, \gamma) = \alpha \times \left| \frac{r_{01}(n_1) + r_{12}(n_1)e^{-i2\beta(n_1,d)}}{1 + r_{01}(n_1)r_{12}(n_1)e^{-i2\beta(n_1,d)}} \right|^2, \tag{5}$$

with

$$d = \gamma \times t, \tag{6}$$

where t is the deposition time and γ is the deposition rate. The refractive indices of the ice samples deposited at different growth temperatures are determined by fitting eqn (5) to the photodiode signal during ice growth.

A quantitative analysis of the thermally induced thickness decrease is possible by determining the ice thickness at different temperatures. This can be achieved by relating the reflected laser light intensity to the ice thickness during thermal annealing. For that purpose we assume that the refractive index obtained for an ice deposited at a specific temperature is applicable to ices deposited at a lower temperature and thermally annealed to that specific temperature. The ice thickness during thermal annealing can then be derived by finding the closest root (d) to the initial ice thickness after deposition (d_1) that satisfies[23]

$$S(d,T) - S_1(d_1,T_1) = 0, \tag{7}$$

where $S(d,T)$ is the photodiode signal at a given thickness d and a specific temperature T, and $S_1(d_1,T_1)$ is the photodiode signal collected at the end of deposition, for which the ice thickness d_1 and the temperature T_1 are known.

2.3 IR spectroscopy

The final H_2O:CO_2 ratio in the solid phase is estimated based on infrared spectroscopy and the integrated absorption coefficients from the literature.[35,40] Infrared spectra are recorded using a Fourier transform infrared spectrometer (Varian 670-IR FTIR) in transmission between 4000 and 400 cm^{-1} with a resolution of 1 cm^{-1}. The infrared beam (not shown in Fig. 1) is aligned along the optical axis that coincides with the line

Table 1 IR band strengths (A_i) of H_2O and $^{13}CO_2$ stretching modes in pure and mixed ices

Ice	Mode	A_i	Ref.
H_2O	O–H stretch	2.0×10^{-16}	1
H_2O:CO_2	O–H stretch	2.1×10^{-16}	2
CO_2	$^{13}C{=}O$ stretch	7.8×10^{-17}	1
H_2O:CO_2	$^{13}C{=}O$ stretch	7.6×10^{-17}	1

References: (1) Gerakines *et al.*;[35] (2) Öberg *et al.*[40]

substrate–photodiode. Consequently it is not possible to perform laser interference and IR spectroscopy experiments simultaneously. A total of 256 interferograms are averaged to improve the S/N ratio. Background spectra are acquired at 20 K prior to sample deposition. The column density of molecules in the ice, N (in molecules cm^{-2}), is derived from the infrared spectra acquired after deposition at 20 K by the relation

$$N = \frac{\ln 10 \times \int A \, d\bar{\nu}}{A_i} \times \cos \theta \tag{8}$$

where $\int A \, d\bar{\nu}$ is the integrated intensity of a particular absorption band and A_i is the corresponding band strength in cm per molecule. The last term in eqn (8) corrects the overestimation of N resulting from the non-orthogonal orientation of the IR beam and the ice sample.[41] Table 1 lists the band strengths for the vibrational modes of H_2O and CO_2 ices (pure and mixed).

3 Results and discussion

3.1 Deposition

Fig. 2 shows an example of an interference fringe pattern (reduced data points) obtained during the deposition of a pure H_2O ice at 20 K. All samples are grown following the same
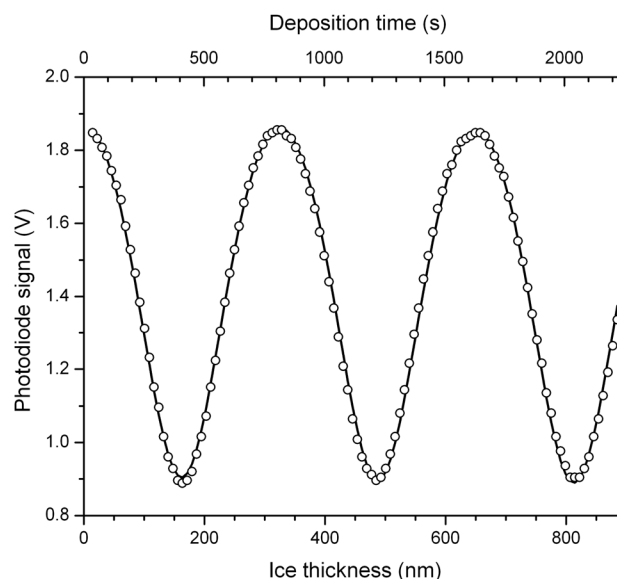

Fig. 2 Optical interference signal during deposition of a pure H_2O ice sample at 20 K (reduced data points, open circles) and the best fit (solid line) using eqn (5). The first and last point indicate the start and the end of the deposition process, respectively.

Table 2 Best set of parameters from fitting eqn (5) to the interference fringe patterns obtained for H_2O, CH_3OH, CO_2 and $H_2O:CO_2 = 2:1$ ice samples grown at different temperatures following background deposition

T [K]	20	30	40	50	60	70	80	90	100	120
H_2O										
n_1	1.188	1.202	1.206	1.210	1.213	1.219	1.224	1.228	1.239	1.259
$1/\alpha$ [V^{-1}]	3.969	3.934	3.901	3.935	4.020	3.986	4.009	3.880	4.004	3.934
γ [nm s^{-1}]	0.412	0.393	0.407	0.393	0.287	0.336	0.337	0.384	0.314	0.283
R^2	0.996	0.997	0.995	0.996	0.994	0.996	0.997	0.996	0.994	0.997
CH_3OH										
n_1	1.249	1.265	1.270	1.275	1.280	1.291	1.320	1.344		
$1/\alpha$ [V^{-1}]	3.941	3.994	3.892	4.018	3.914	3.928	3.886	4.064		
γ [nm s^{-1}]	0.289	0.285	0.287	0.247	0.223	0.243	0.214	0.217		
R^2	0.995	0.994	0.995	0.995	0.995	0.996	0.996	0.997		
CO_2										
n_1	1.221	1.257	1.278	1.315	1.313	1.309				
$1/\alpha$ [V^{-1}]	3.854	3.864	3.809	3.842	3.790	3.780				
γ [nm s^{-1}]	0.289	0.285	0.287	0.247	0.223	0.243				
R^2	0.995	0.994	0.995	0.995	0.995	0.996				
$H_2O:CO_2 = 2:1$[a]										
n_1		1.248	1.274	1.299	1.300	1.291				
$1/\alpha$ [V^{-1}]		3.951	3.939	3.860	3.854	3.904				
γ [nm s^{-1}]		0.317	0.263	0.239	0.266	0.256				
R^2		0.998	0.998	0.997	0.996	0.995				

[a] Values taken from Bossa et al.[42]

protocol: the deposition is always stopped at a point with maximum sensitivity to changes in ice thickness, e.g., when the signal is located at an upward slope, e.g., half-way between the third destructive interference and the third constructive interference (see also Bossa et al.[23]). This results in a final ice thickness ranging between 0.8 and 0.9 μm (∼3000 MLs). Changes in the interference signal thus correspond directly to changes in ice thickness, simplifying real-time interpretation of the results. For all ice samples, the periodicity of the interference fringe patterns indicates a fairly constant growth rate with <5% variation in the half-period. Furthermore, we observe that the amplitude of the interference fringes slightly decreases during the deposition, likely due to an increasing loss of photons through scattering effects. This amplitude damping is at maximum 2%.

The solid line in Fig. 2 shows the best fit of eqn (5) to the interference fringe pattern. The fitted region is determined by the experimentally noted start and end of deposition. The best set of parameters for H_2O, CH_3OH, CO_2 and $H_2O:CO_2 = 2:1$ ice samples deposited at different growth temperatures is given in Table 2. Fig. 3 shows the *coefficient of the determination* plot describing the goodness of the fit for a pure H_2O ice sample deposited at 20 K. A unique R^2 maximum demonstrates that the fit has found a set of parameters (n_1, α and γ) that corresponds to a global minimum.

3.2 Refractive indices and deposition rates

The left panel of Fig. 4 shows the complex refractive indices (full circles) obtained for H_2O, CH_3OH, CO_2 and $H_2O:CO_2 = 2:1$ ice samples as a function of the growth temperature. The laser light absorption from the ices is assumed to be negligible and the imaginary component of the refractive indices is
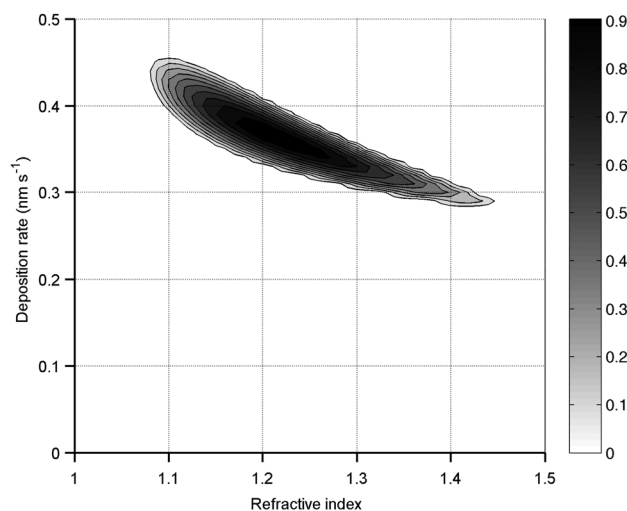

Fig. 3 Coefficient of determination (R^2, color bar) from the fits using eqn (5) for a pure H_2O ice sample deposited at 20 K as a function of the refractive index n_1, and the deposition rate γ, with the scaling factor α fixed to an optimised value.

approximately zero.[15,42] In the case of H_2O, we consider the 20–120 K growth temperature range in which H_2O vapour deposition onto the cold silicon substrate results in an amorphous ice.[21,23] Under our experimental conditions pure CH_3OH ice crystallises between 105 and 125 K limiting the presented data up to 90 K. Beyond 70 K, CO_2 molecules desorb from a H_2O ice matrix.

The refractive indices of pure H_2O ice samples are in good agreement with previously published values[15,43] and we observe an increase of the refractive index with the growth temperature. In contrast to Dohnálek et al.[15] whose data set comprises
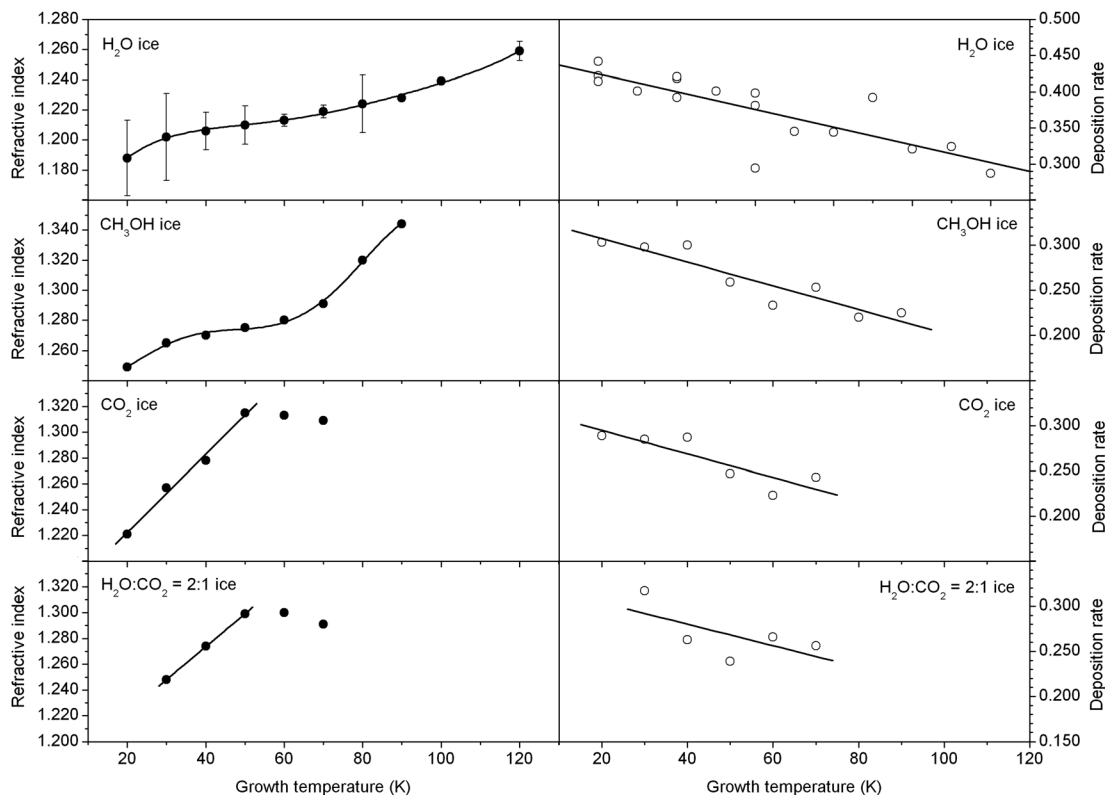
Fig. 4 Refractive indices (full circles) and deposition rates (open circles) obtained for H_2O, CH_3OH, CO_2 and $H_2O : CO_2 = 2 : 1$ ice samples as a function of the growth temperature. The polynomial and linear fits are shown as solid lines. The error bars (top left panel) are representative of the repeatability of the procedure at the 95% confidence level.

less points, the observed increase is not fully linear; a fifth order polynomial function – that is used in Section 3.4 to quantify the thickness decrease – reproduces better the trend. This nonlinearity has also been observed in a previous study,[36] however with small deviations from the refractive indices concluded from our measurements. This can be explained by different experimental conditions such as the deposition rates. We have checked the repeatability of the experimental procedure with H_2O: the data points shown at 20–90 K, 100 K and 120 K have been repeated up to four times and gave a mean error of about 1%. An initial set of measurements (Isokoski 2013, PhD thesis) reproduces well all data above 50 K, but finds somewhat off-set values at lower temperatures and this is not fully understood. At this stage, we take all these values into account, resulting in larger errors for 20, 30, 40 and 50 K. For the pure CH_3OH ice samples, the refractive indices also increase with the growth temperature. The increase is however more pronounced beyond 60 K and the refractive indices are in general higher than those of H_2O. For the pure CO_2 ice samples, the refractive indices increase linearly with the temperature, reaching a maximum at 50 K. Beyond 50 K, the refractive indices slightly decrease towards 70 K. The refractive indices obtained for $H_2O : CO_2 = 2 : 1$ ice samples resemble that of pure CO_2 ice samples.

The right panel of Fig. 4 shows the deposition rates (open circles) obtained for all ices. In general we observe that the

deposition rates decrease nearly linearly with the growth temperature indicating that (i) the sticking coefficient of the different molecules decreases with increasing growth temperature, and (ii) ices are getting more dense with increasing growth temperature: higher density requires more molecules per unit volume, which for a constant deposition rate manifests itself as a slower ice growth rate. Following equivalent deposition procedures, CH_3OH and CO_2 ices grow much slower than H_2O ices, likely due to the different masses and volatilities. The co-deposited CO_2 influences the deposition rate of the condensing $H_2O : CO_2 = 2 : 1$ ice sample as well, resulting in a slower process compared to pure water.

3.3 Thermal annealing

Fig. 5 shows the laser interference signal during thermal annealing of H_2O, CH_3OH, CO_2 and $H_2O : CO_2 = 2 : 1$ ice samples deposited at different growth temperatures. The starting point here coincides with the end of deposition, *i.e.*, the last point of the interference fringe pattern as seen in Fig. 2. For the H_2O ice sample deposited at 20 K, the signal decreases gradually as the temperature increases. An inflexion point is observed between 40 and 50 K, probably related to the phase transition in ASW from its high-density (I_{hda}) to its low-density (I_{lda}) form, which takes place at 38–68 K.[44] From 50 K onwards, the gradual decrease in the signal continues. The signal drops noticeably at around 150 K, matching the
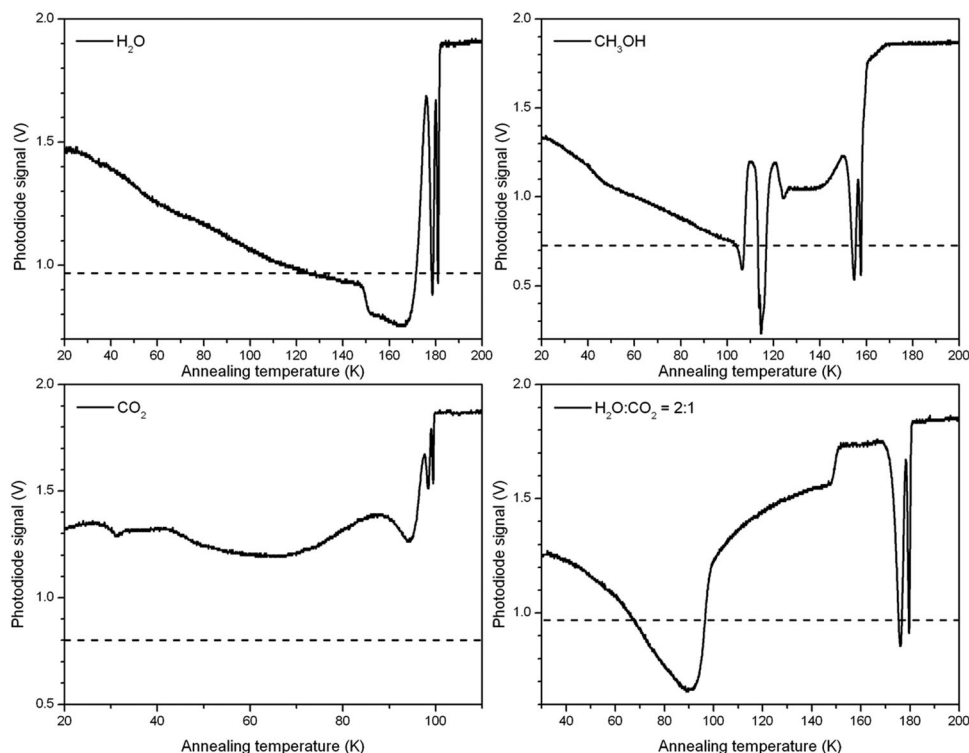
3460 | *Phys. Chem. Chem. Phys.*, 2014, **16**, 3456–3465

This journal is © the Owner Societies 2014

Fig. 5 Interference signal during thermal annealing or H_2O, CH_3OH, CO_2 and $H_2O : CO_2 = 2 : 1$ ice samples. The dashed line indicates the lowest signal obtained during the initial deposition.

crystallisation temperature.[45] Thermal stresses and density variations during phase transitions trigger cracks within the ice that cause light scattering.[4] An exothermic amorphous to crystalline phase transition may also release some molecules in the gas phase, explaining the signal drop. We observe a similar signal drop up to ~100 K followed by signal fluctuations for CH_3OH between 105 K and 125 K. The signal fluctuations are likely due to successive phase transitions within the ice that are generally related to intermolecular forces that – in the case of CH_3OH – differ with the growth temperature.[46,47] An inflexion point is also observed for CH_3OH between 40 and 50 K. For pure CO_2 ice, which crystallises between 35 and 50 K,[48] the interference signal remains relatively constant until 90 K. For the $H_2O : CO_2 = 2 : 1$ ice sample deposited at 30 K, the signal decreases continuously to about 90 K, coincident with the desorption temperature of pure CO_2. The crystallisation temperature of pure H_2O is then observed at 150 K. During desorption, all signals cycle back through the interference fringes as the different ices become thinner. The signals generally dive below the level of complete destructive interference (depicted as dashed lines in Fig. 5). A signal smaller than this threshold can only be explained by a loss of photons.

3.4 Thickness decrease

By solving eqn (7) from the drop in signal and by taking into account the change in refractive index with temperature, we can provide a quantitative analysis of the observed thickness decrease from the growth temperature up to near the crystallisation temperature for all ice samples. For pure CO_2 ice, the thickness is derived between 20 and 50 K only, as possible changes in the surface reflectance after crystallisation prohibit interpretation above 50 K. The same reasoning limits the analysis of the $H_2O : CO_2 = 2 : 1$ and H_2O ice data to 50 and 120 K, respectively. Fig. 6 shows the thermal evolution of the calculated thickness in H_2O, CH_3OH, CO_2 and $H_2O : CO_2 = 2 : 1$ ices deposited at 20 K. Both H_2O and CH_3OH ices show periods of rapid and slow collapse. Slow collapse occurs at around 40 K for H_2O and at around 50 K for CH_3OH. The $H_2O : CO_2 = 2 : 1$ and CO_2 ice thicknesses decrease linearly with temperature over the studied temperature range. The total thinning for pure H_2O between 20 and 120 K is around 12%. The value for pure CH_3OH ice between 20 and 90 K is around 14%. Pure CO_2 and $H_2O : CO_2 = 2 : 1$ ices show a decrease of about 10 and 6% between 20 and 50 K.

The confidence intervals obtained for each parameter of the polynomial and linear fits provide an error estimation of the total thickness decrease. Fig. 7 shows the total thickness decrease (in %) of pure H_2O and CH_3OH ice samples deposited at different growth temperatures, and then thermally annealed to 120 K and 90 K, respectively. For both ices, the total structural collapse decreases linearly with the growth temperature. By extrapolating these data, we observe that ices grown near their crystallisation temperature are compact and the total thickness decrease equals zero, which is in good agreement with previous experimental studies.[15,23,44,49]
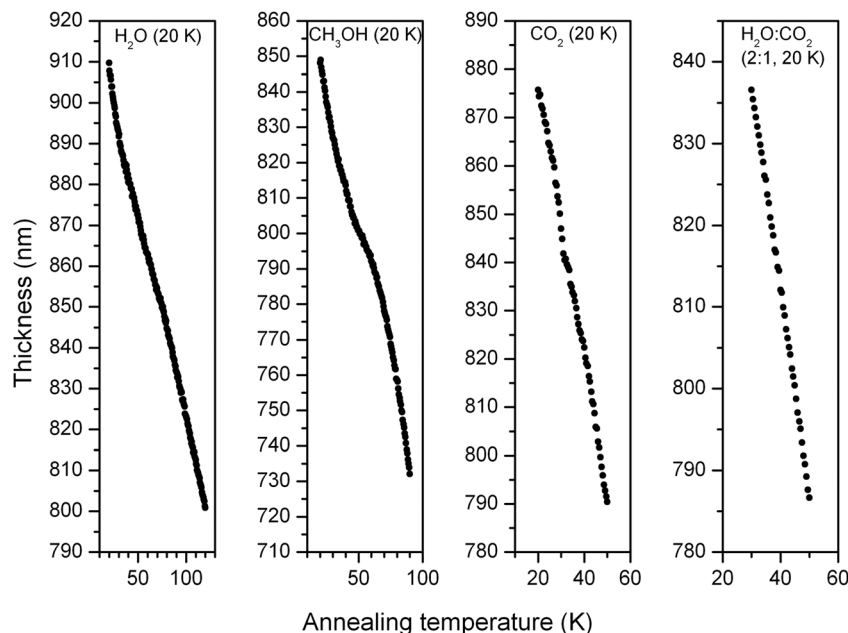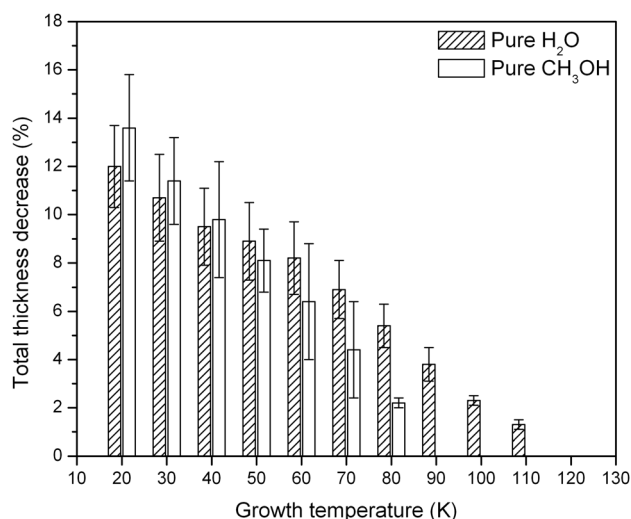
Fig. 6   Thickness decrease upon thermal annealing of H_2O, CH_3OH, CO_2 ice deposited at 20 K and $H_2O : CO_2 = 2 : 1$ ice deposited at 30 K. Note that the thickness and temperature ranges are not equal.

Fig. 7   Total thickness decrease (in %) of pure H_2O and CH_3OH ice samples deposited at different growth temperatures and then thermally annealed to 120 K and 90 K, respectively.

3.5   Residual porosity in annealed H_2O

From the Lorentz–Lorenz equation, we can relate each measured refractive index n_1 to the initial porosity p and the initial density ρ, i.e., the porosity and the density of the ice before thermal annealing[15,38,50]

$$p = 1 - \left(\frac{n_1^2 - 1}{n_1^2 + 2} \times \frac{n_i^2 + 2}{n_i^2 - 1} \right) = 1 - \frac{\rho}{\rho_c}, \qquad (9)$$

with $n_i = 1.285$, the intrinsic refractive index of H_2O ice (i.e., not including pores)[15] and $\rho_c = 0.94$ g cm^{-3}, the intrinsic density of

compact H_2O ice.[51] By assuming a one dimensional structural collapse, we also assume an direct inverse correlation between thickness decrease and density increase. Fig. 8 shows that porous H_2O ice samples deposited below 110 K and annealed to 120 K never reach the intrinsic density of compact H_2O ice, meaning that pores are not fully destroyed during the thermal annealing.
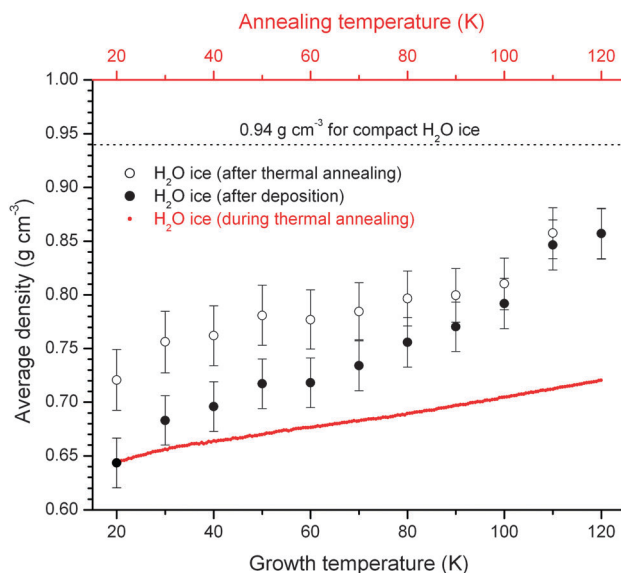

Fig. 8   Average density of porous H_2O ice samples after deposition (black circles) and after thermal annealing to 120 K (open circles). Black and open circles for one specific temperature show the start and end point during an annealing experiment, respectively. This is illustrated by the red line for one selected measurement of a porous H_2O ice sample grown at 20 K and heated with 2 K min^{-1}, showing the average density as a function of the annealing temperature (upper x-axis).

The persistence of porosity upon thermal annealing poses a contradiction to the original approximation that the refractive index is the same for both the ice deposited at a specific temperature, and the one annealed to that temperature. However, since the annealing experiment (driven by the heating rate) is faster than the pure water ice reorganisation (driven by the diffusion of the water molecules),[52,53] our original approximation is more applicable to longer time scales. The isothermal thickness decrease under ultra-high vacuum conditions should be investigated in future experiments. Given the annealing experiment time scale, an underestimation of the porosity results in an overestimation of the density/refractive index. This translates into an overestimation of the total thickness decrease. Therefore, the values given in Fig. 7 should be considered as upper limits. Since the initial porosity depends on the growth temperature, the overestimation is likely to be highest for ices grown at the lowest temperatures. H_2O ice containing large pores (2–50 nm) has been shown to retain a third of the original porosity beyond crystallisation.[54] These cavities remaining at high temperatures are not visible through IR spectroscopy of the dangling O–H bonds, which disappear before crystallisation. This has been interpreted as either coalescence of smaller pores into larger pores, preferential destruction of small pores or decrease of surface roughness of the pores.[50,54] Our results support this picture and suggest that omnidirectional background deposition of H_2O – applicable to the vapor deposition in the ISM – possibly results in larger pores sustained in the ice upon thermal annealing. A comparison with the CH_3OH ice samples is not possible since the intrinsic refractive index of CH_3OH ice (*i.e.*, not including pores) is lacking.

3.6 Segregation of CO_2 in annealed $H_2O:CO_2 = 2:1$

Segregation of ice components is typical for thermally annealed H_2O ices containing CO_2. Segregation of CO_2 in a water environment starts above 40 K and ends when the segregated material desorbs. It is evidenced by the appearance of infrared features characteristic of pure CO_2 ice.[55–58] In particular, the CO_2 ($\nu_1 + \nu_3$) combination and ($2\nu_2 + \nu_3$) combination/overtone bands are sensitive to the matrix environment.[11] While these bands are visible for the $H_2O:CO_2 = 2:1$ ice at all temperatures, sharper peaks appear from 60 K onwards at 3708 and 3600 cm^{-1} (see example in Fig. 9), characteristic of pure CO_2 ice,[59] and consistent with a segregation process in which H_2O and CO_2 separate. Fig. 10 shows the pure CO_2 fraction in $H_2O:CO_2 = 2:1$ ice deposited at 20 K, then warmed up to 120 K for porous and compact ices. Both ices come from the same gas mixture, deposited at 20 K following the background deposition procedure for the porous one and using a gas inlet directed toward the silicon substrate at normal incidence for the compact one. The amount of CO_2 ice that is segregated is calculated from 40 to 100 K by fitting a pure CO_2 ice spectrum (porous or compact) and a $H_2O:CO_2 = 2:1$ ice spectrum (porous or compact) to the segregating ice.[58] An example is given in Fig. 9. The reference spectra (porous and compact) are acquired at 40 K, the temperature at which the kinetics of segregation is too slow to occur. Both environment and temperature discrepancies induce
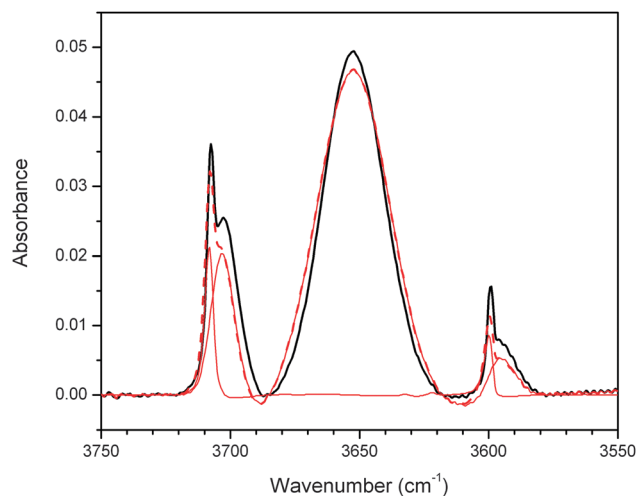

Fig. 9 Example of an infrared spectrum of $H_2O:CO_2 = 2:1$ deposited at 20 K then warmed up to 70 K (black line), fitted with a porous CO_2 ice spectrum and a porous $H_2O:CO_2$ ice spectrum background deposited at 40 K (red solid lines). The combined fit is the red dashed line.
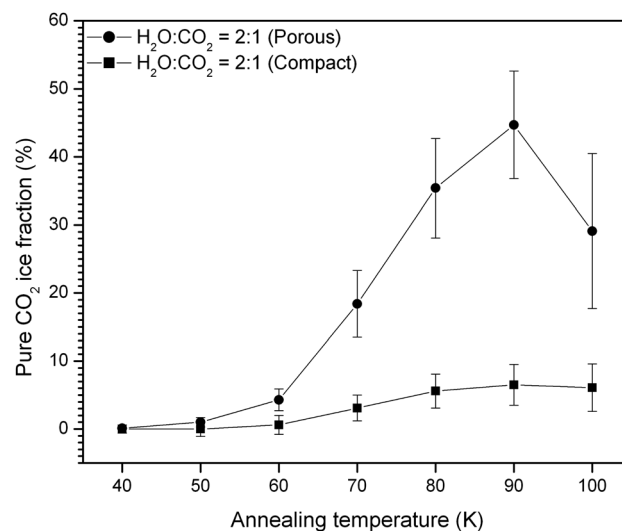

Fig. 10 Pure CO_2 ice fraction (in percent) in the $H_2O:CO_2 = 2:1$ ice sample upon thermal annealing for porous ice (circles) and compact ice (squares).

residuals in the fits. We use the confidence intervals obtained for each parameter to estimate the error in the fraction obtained. We observe that the amount of segregated material during the thermal annealing strongly depends on the initial porosity: the pure CO_2 ice fraction reaches about 45% at 90 K for an initial porous ice in contrast to about 6.5% for an initial compact ice at the same temperature. Using infrared spectroscopy, we observe segregation starting beyond 50 K, independently of the initial ice morphology. Clearly, a high initial porosity leads to a higher extent of CO_2 segregation.

3.7 Astrophysical implications

The structural collapse of H_2O, CH_3OH, CO_2 and mixed $H_2O:CO_2 = 2:1$ ice – upon heating is not large in terms of

This journal is © the Owner Societies 2014

Phys. Chem. Chem. Phys., 2014, **16**, 3456–3465 | **3463**

thickness but a decrease of the order of 6–14% may correspond to a substantial loss in terms of specific surface area. The persistence of porosity upon thermal annealing during the laboratory time scale is favourable for surface reactions since reaction sites remain available until water crystallisation. However, for longer times scales, we expect the number of reaction sites to become scarce due to low temperature water ice reorganisation.[52,53] On the other hand, a low temperature structural collapse may facilitate the diffusion of adsorbates which are in principle limited by their mass and their binding energy[25] demonstrated that the thermal processing of porous ASW leads to a marked enhancement of low temperature acid–base reaction yields, in contrast to compact ASW. This is in line with the results found here. We find that the initial porosity of an ice mixture affects the efficiency of the ice segregation. Therefore, the initial porosity of an ice mixture, the diffusion coefficients of individual adsorbates and the low temperature water ice reorganisation may strongly affect the solid state formation rates of complex organic molecules. These three parameters should be taken into account in astrochemical models.

4 Summary and conclusions

We have studied the thickness decrease of H_2O, CH_3OH, CO_2 and $H_2O : CO_2 = 2 : 1$ ice samples upon thermal annealing in an astronomically relevant temperature range. Using laser optical interference together with FTIR spectroscopy, we have found the following:

(1) Porous H_2O ice undergoes a gradual thermal collapse throughout the amorphous regime. A total thinning of about 12% is derived between 20 and 120 K. This value is an upper limit.

(2) Porous H_2O ice is not fully compacted during the thermal annealing experiment time scale. Depending on the growth temperature, the residual porosity after annealing to 120 K can reach 17 ± 3%. Large cavities remain in the ice throughout the solid phase, not observable though infrared spectroscopy of dangling OH bonds.

(3) The initial porosity of the ice determines its structure throughout the solid phase until ice evaporation. H_2O rich ices formed by vapor deposition on cold interstellar dust grains may contain large cavities that persist over a large temperature range, and affect the catalytic potential of the ice as well as the trapping of gases.

(4) A high initial porosity leads to a higher extent of CO_2 segregation.

Acknowledgements

References

1 D. C. B. Whittet, P. A. Gerakines, A. G. G. M. Tielens, A. J. Adamson, A. C. A. Boogert, J. E. Chiar, T. de Graauw, P. Ehrenfreund, T. Prusti, W. A. Schutte, B. Vandenbussche and E. F. van Dishoeck, *Astrophys. J., Lett.*, 1998, **498**, L159.

2 K. M. Pontoppidan, A. C. A. Boogert, H. J. Fraser, E. F. van Dishoeck, G. A. Blake, F. Lahuis, K. I. Öberg, N. J. Evans II and C. Salyk, *Astrophys. J.*, 2008, **678**, 1005.

3 K. I. Öberg, A. C. A. Boogert, K. M. Pontoppidan, S. van den Broek, E. F. van Dishoeck, S. Bottinelli, G. A. Blake and N. J. Evans II, *Astrophys. J.*, 2011, **740**, 109.

4 R. A. Baragiola, *Planet. Space Sci.*, 2003, **51**, 953–961.

5 T. Loerting, K. Winkel, M. Seidl, M. Bauer, C. Mitterdorfer, P. H. Handle, C. G. Salzmann, E. Mayer, J. L. Finney and D. T. Bowron, *Phys. Chem. Chem. Phys.*, 2011, **13**, 8783.

6 E. Mayer and R. Pletzer, *Nature*, 1986, **319**, 298–301.

7 A. Bar-Nun, J. Dror, E. Kochavi and D. Laufer, *Phys. Rev. B: Condens. Matter Mater. Phys.*, 1987, **35**, 2427–2435.

8 P. Ayotte, R. S. Smith, K. P. Stevenson, Z. Dohnálek, G. A. Kimmel and B. D. Kay, *JGR, J. Geophys. Res., Planets*, 2001, **106**, 33387–33392.

9 M. P. Collings, J. W. Dever, H. J. Fraser, M. R. S. McCoustra and D. A. Williams, *Astrophys. J.*, 2003, **583**, 1058–1062.

10 A. Bar-Nun, D. Laufer, O. Rebolledo, S. Malyk, H. Reisler and C. Wittig, in *Gas Trapping in Ice and Its Release upon Warming*, ed. M. S. Gudipati and J. Castillo-Rogez, 2013, p. 487.

11 J. V. Keane, A. C. A. Boogert, A. G. G. M. Tielens, P. Ehrenfreund and W. A. Schutte, *Astron. Astrophys.*, 2001, **375**, L43–L46.

12 E. L. Gibb, D. C. B. Whittet, A. C. A. Boogert and A. G. G. M. Tielens, *Astrophys. J., Suppl. Ser.*, 2004, **151**, 35–73.

13 Y. Oba, N. Miyauchi, H. Hidaka, T. Chigai, N. Watanabe and A. Kouchi, *Astrophys. J.*, 2009, **701**, 464–470.

14 K. P. Stevenson, G. A. Kimmel, Z. Dohnálek, R. S. Smith and B. D. Kay, *Science*, 1999, **283**, 1505.

15 Z. Dohnálek, G. A. Kimmel, P. Ayotte, R. S. Smith and B. D. Kay, *J. Chem. Phys.*, 2003, **118**, 364–372.

16 D. A. Williams, T. W. Hartquist and D. C. B. Whittet, *Mon. Not. R. Astron. Soc.*, 1992, **258**, 599–601.

17 R. Papoular, *Mon. Not. R. Astron. Soc.*, 2005, **362**, 489–497.

18 D. H. Wooden, D. E. Harker and A. J. Brearley, *Chondrites and the Protoplanetary Disk*, 2005, p. 774.

19 A. Bar-Nun and T. Owen, *Solar System Ices*, 1998, p. 353.

20 M. E. Palumbo, *Astron. Astrophys.*, 2006, **453**, 903–909.

21 U. Raut, M. Famá, M. J. Loeffler and R. A. Baragiola, *Astrophys. J.*, 2008, **687**, 1070–1074.

22 M. E. Palumbo, G. A. Baratta, G. Leto and G. Strazzulla, *J. Mol. Struct.*, 2010, **972**, 64–67.

23 J.-B. Bossa, K. Isokoski, M. S. de Valois and H. Linnartz, *Astron. Astrophys.*, 2012, **545**, A82.

24 A. Kouchi and T. Yamamoto, *Prog. Cryst. Growth Charact. Mater.*, 1995, **290**, 1009–1018.

25 O. Gálvez, B. Maté, V. J. Herrero and R. Escribano, *Astrophys. J.*, 2010, **724**, 539–545.

26 E. Dartois, W. Schutte, T. R. Geballe, K. Demyk, P. Ehrenfreund and L. D'Hendecourt, *Astron. Astrophys.*, 1999, **342**, L32–L35.

27 K. M. Pontoppidan, E. Dartois, E. F. van Dishoeck, W.-F. Thi and L. d'Hendecourt, *Astron. Astrophys.*, 2003, **404**, L17–L20.

28 K. I. Öberg, R. T. Garrod, E. F. van Dishoeck and H. Linnartz, *Astron. Astrophys.*, 2009, **504**, 891–913.

29 J. K. Jørgensen, C. Favre, S. E. Bisschop, T. L. Bourke, E. F. van Dishoeck and M. Schmalzl, *Astrophys. J., Lett.*, 2012, **757**, L4.

30 N. Watanabe and A. Kouchi, *Astrophys. J., Lett.*, 2002, **571**, L173–L176.

31 G. W. Fuchs, H. M. Cuppen, S. Ioppolo, C. Romanzin, S. E. Bisschop, S. Andersson, E. F. van Dishoeck and H. Linnartz, *Astrophys. J.*, 2009, **505**, 629–639.

32 H. M. Cuppen, E. M. Penteado, K. Isokoski, N. van der Marel and H. Linnartz, *Mon. Not. R. Astron. Soc.*, 2011, **417**, 2809–2816.

33 S. Ioppolo, I. Sangiorgio, G. A. Baratta and M. E. Palumbo, *Astron. Astrophys.*, 2013, **554**, A34.

34 K. Isokoski, C. A. Poteet and H. Linnartz, *Astron. Astrophys.*, 2013, **555**, A85.

35 P. A. Gerakines, W. A. Schutte, J. M. Greenberg and E. F. van Dishoeck, *Astron. Astrophys.*, 1995, **296**, 810.

36 D. E. Brown, S. M. George, C. Huang, E. K. L. Wong, K. B. Rider, R. S. Smith and B. D. Kay, *J. Phys. Chem.*, 1996, **100**, 4988–4995.

37 M. A. Zondlo, T. B. Onasch, M. S. Warshawsky, M. A. Tolbert, G. Mallick, P. Arentz and M. S. Robinson, *J. Phys. Chem. B*, 1997, **101**, 10887.

38 M. S. Westley, G. A. Baratta and R. A. Baragiola, *J. Chem. Phys.*, 1998, **108**, 3321–3326.

39 P. Mottier and S. Valette, *Appl. Opt.*, 1981, **20**, 1630–1634.

40 K. I. Öberg, H. J. Fraser, A. C. A. Boogert, S. E. Bisschop, G. W. Fuchs, E. F. van Dishoeck and H. Linnartz, *Astron. Astrophys.*, 2007, **462**, 1187–1198.

41 C. J. Bennett, C. Jamieson, A. M. Mebel and R. I. Kaiser, *Phys. Chem. Chem. Phys.*, 2004, **6**, 735.

42 J.-B. Bossa, K. Isokoski, D. M. Paardekooper, M. Bonnin, E. P. van der Linden, T. Triemstra, S. Cazaux, A. G. G. M. Tielens

and H. Linnartz, *Astron. Astrophys.*, 2013, DOI: 10.1051/0004-6361/201322549.

43 B. S. Berland, D. E. Brown, M. A. Tolbert and S. M. George, *Geophys. Res. Lett.*, 1995, **22**, 3493–3496.

44 P. Jenniskens and D. F. Blake, *Science*, 1994, **265**, 753–756.

45 R. Scott Smith, T. Zubkov and B. D. Kay, *J. Chem. Phys.*, 2006, **124**, 114710.

46 D. Ehlers, *Surf. Sci.*, 1985, **160**, 57–69.

47 A. Bolina, A. Wolff and W. Brown, *J. Chem. Phys.*, 2005, **122**, 44713.

48 M. Falk, *J. Chem. Phys.*, 1987, **86**, 560–564.

49 R. Scott Smith, *Surf. Sci.*, 1996, **367**, L13–L18.

50 U. Raut, B. D. Teolis, M. J. Loeffler, R. A. Vidal, M. Famá and R. A. Baragiola, *J. Chem. Phys.*, 2007, **126**, 244511.

51 A. H. Narten, C. G. Venkatesh and S. A. Rice, *J. Chem. Phys.*, 1976, **64**, 1106–1121.

52 B. Maté, Y. Rodrguez-Lazcano and V. J. Herrero, *Phys. Chem. Chem. Phys.*, 2012, **14**, 10595.

53 F. Mispelaer, P. Theulé, H. Aouididi, J. Noble, F. Duvernay, G. Danger, P. Roubin, O. Morata, T. Hasegawa and T. Chiavassa, *Astron. Astrophys.*, 2013, **555**, A13.

54 U. Raut, M. Famá, B. D. Teolis and R. A. Baragiola, *J. Chem. Phys.*, 2007, **127**, 204713.

55 A. C. A. Boogert, P. Ehrenfreund, P. A. Gerakines, A. G. G. M. Tielens, D. C. B. Whittet, W. A. Schutte, E. F. van Dishoeck, T. de Graauw, L. Decin and T. Prusti, *Astron. Astrophys.*, 2000, **353**, 349–362.

56 M. E. Palumbo and G. A. Baratta, *Astron. Astrophys.*, 2000, **361**, 298–302.

57 R. Hodyss, P. V. Johnson, G. E. Orzechowska, J. D. Goguen and I. Kanik, *Icarus*, 2008, **194**, 836–842.

58 K. I. Öberg, E. C. Fayolle, H. M. Cuppen, E. F. van Dishoeck and H. Linnartz, *Astron. Astrophys.*, 2009, **505**, 183–194.

59 S. A. Sandford and L. J. Allamandola, *Astrophys. J.*, 1990, **355**, 357–372.

This journal is © the Owner Societies 2014

Phys. Chem. Chem. Phys., 2014, **16**, 3456–3465 | **3465**